JACS Au
AN OPEN ACCESS JOURNAL OF THE AMERICAN CHEMICAL SOCIETY

pubs.acs.org/jacsau
Article

Site-Specific Cascade-Activatable Fluorogenic Nanomicelles Enable Precision and Accuracy Imaging of Pulmonary Metastatic Tumor

Xueqian Chen, Jiatian Liu, Yong Zhang, Xueyun Gao,* and Dongdong Su*

Cite This: JACS Au 2024, 4, 2606−2616
Read Online

ACCESS | Metrics & More | Article Recommendations | Supporting Information

ABSTRACT: The precise localization of metastatic tumors with subtle growth is crucial for timely intervention and improvement of tumor prognosis but remains a paramount challenging. To date, site-specific activation of fluorogenic probes for single-stimulus-based diagnosis typically targets an occult molecular event in a complex biosystem with limited specificity. Herein, we propose a highly specific site-specific cascade-activated strategy to enhance detection accuracy, aiming to achieve the accurate detection of breast cancer (BC) lung metastasis in a cascade manner. Specifically, cascade-activatable NIR fluorogenic nanomicelles **HPNs** were constructed using ultra-pH-sensitive (UPS) block copolymers as carriers and nitroreductase (NTR)-activated fluorogenic reporters. **HPNs** exhibit programmable cascade response characteristics by first instantaneous dissociating under *in situ* tumor acidity, facilitating deep tumor penetration followed by selective fluorescence activation through NTR-mediated enzymatic reaction resulting in high fluorescence ON/OFF contrast. Notably, this unique feature of **HPNs** enables high-precision diagnosis of orthotopic BC as well as its lung metastases with a remarkable signal-to-background ratio (SBR). This proposed site-specific cascade activation strategy will offer opportunities for a specific diagnosis with high signal fidelity of various insidious metastatic lesions *in situ* across different diseases.

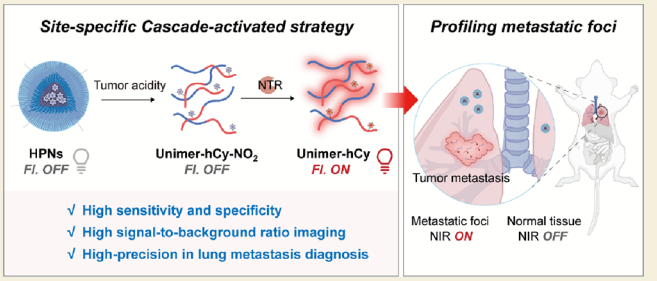

KEYWORDS: *Imaging, cascade activation, NIR fluorogenic nanomicelles, lung metastasis, precise diagnosis*

INTRODUCTION

Breast cancer (BC) is characterized by its high aggressiveness and metastasis rate.[1−3] Lung metastasis is a common complication of BC, accounting for approximately 50% of cases, which contributes to the alarmingly high morbidity and mortality.[4−7] Therefore, there is an urgent need to develop advanced diagnostic tools for specific detection of BC lung metastases in order to facilitate timely intervention and effective treatment. However, the random distribution of tumor metastasis poses a significant challenge for clinical therapy and operation.[8−11] Biopsy aimed at histopathologic determination of BC faces limitations due to its invasiveness and incomplete identification of metastatic lesions.[12] Furthermore, accurate detection and localization of BC lung metastases remain formidable tasks due to their small size, limited contrast, and indistinct boundaries with neighboring normal tissues.[10,13]

The development of site-specific activation fluorogenic probes has significantly enhanced the sensitive identification of tumors, enabling precise detection and localization of tumor metastases with a high signal-to-background ratio (SBR).[14−18] However, most activatable fluorogenic probes are limited to a single stimulus, rendering them vulnerable to physiological and pathological fluctuations and compromising their accuracy in distinguishing underdiagnosed lung metastases. To overcome this limitation, multistimuli-activatable fluorogenic probes have been proposed, which can intelligently respond to multiple specific indicators to produce a low-background and specific imaging signal compared to single-stimulus probes.[19−25]

A site-specific cascade-activated strategy that offers tunable properties (such as size- and charge-switchable behavior, activatable fluorescence) in response to tumor environmental stimuli would enable specific and accurate diagnosis of hidden metastases foci.[26−30] Notably, the presence of primary site efficiently obstructs the activation of secondary site, thereby preventing premature activation by low-level indicators present in normal tissues before accumulation of imaging agents in tumors.[31−33] Therefore, the site-specific cascade-activatable fluorogenic probes allow for a fluorescence response to orthogonal indicators *in situ*, facilitating highly specific and sensitive diagnostic imaging of elusive lung metastases.

Ultra-pH-sensitive (UPS) nanomicelles have demonstrated their remarkable potential as efficient carriers for pH-

Received: April 19, 2024
Revised: June 3, 2024
Accepted: June 10, 2024
Published: June 24, 2024

https://doi.org/10.1021/jacsau.4c00356
JACS Au 2024, 4, 2606−2616

Scheme 1. Schematic Illustration of Site-Specific Cascade-Activatable Fluorogenic Nanomicelles HPNs for Programmable Targeting and Precise Detection of Pulmonary Metastatic Tumor[a]

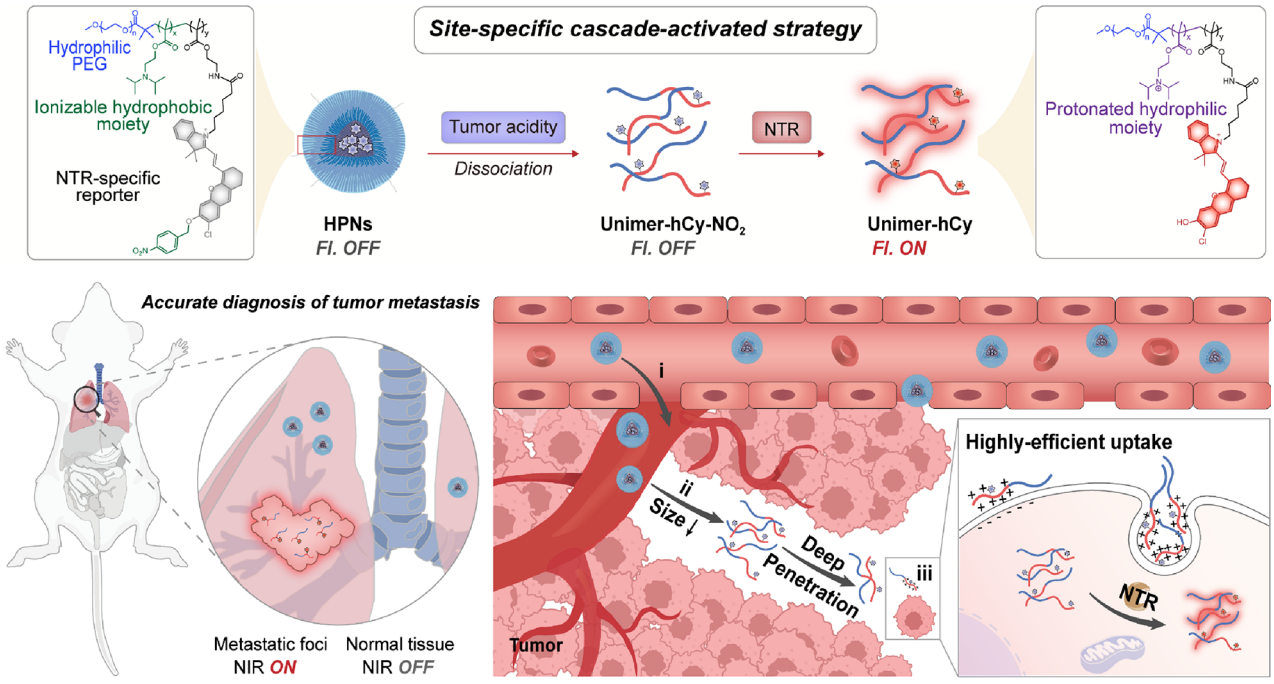

[a](i) **HPNs** with an initially large nanomicelle morphology exhibit prolonged blood circulation time and preferential accumulation in tumor tissue via EPR effect. (ii) Upon deposition in the acidic tumor microenvironment, **HPNs** undergo instantaneous size-switchable behavior, dissociating into small-sized unimers to facilitate deep tumor penetration followed by the exposure of the caged **hCy-NO$_2$** reporter. (iii) Subsequently, due to acid-triggered protonation and dissociation of **HPNs**, the resulting unimers efficiently enter tumor cells, promoting intracellular fluorescence activation by NTR and enabling high SBR imaging of BC lung metastasis.

responsive tumor delivery. Unlike previous pH-activatable probes with a broad response range,[34−36] UPS block nanomicelles contain tertiary amine blocks that exhibit sensitivity to subtle changes in pH, enabling amphiphilic conversion and a sharp pH range for nanomicelle disassembly. Importantly, currently available UPS nanomicelles exhibit a narrow pH$_e$ range and tunable pK_a, making them suitable for distinguishing tumor extracellular acidity (pH$_e$ 6.5−7.0) from healthy tissues (pH$_e$ 7.2−7.4).[37,38] Meanwhile, PEGylated nanomicelles offer improved metabolic kinetics, enhancing the *in situ* accumulation of fluorescent probes in solid tumors and enabling the sensitivity and specific diagnosis of tumor metastasis.

To enhance the imaging accuracy and SBR of hard-to-locate micrometastases, more precise cascade activation strategies can be designed by incorporating a secondary tumor-specific indicator. Nitroreductase (NTR) is an aberrantly expressed biomarker for hypoxia in various solid tumors, which not only directly correlates with the degree of hypoxia but also plays a role in the growth and metastasis of tumor cells.[39−42] Several NTR-activatable NIR fluorescent probes have been reported for diagnosing metastatic tumors.[39,42] Jiang et al. developed a macromolecular NIR PEG-conjugated iridium(III) complex that effectively detects primary tumors and small liver metastatic nodules measuring approximately 1 mm, by specifically responding to tumor acidity and hypoxia.[20] Drawing inspiration from these concepts, we propose that combining tumor extracellular acidity pH$_e$ with NTR can effectively address this challenge, thereby significantly expanding the potential application of programmable responsive nanoprobe imaging technology in detecting micrometastatic tumors. Particularly in complex organisms, the development of costimulatory probes offers significant potential for precise imaging and discrimination of BC lung metastases.

The proposed diagnostic probe for BC lung metastases should possess the following typical characteristics: (i) an appropriate pK_a and ultrasensitive response to subtle pH chances, specifically matching the extracellular pH of lung metastases, and (ii) *in situ* cascade activation to ensure accurate imaging and enhanced SBR of tiny lesions. In this study, we developed a cascade-activatable nanoprobe called **HPNs** that can logically respond to two orthogonal stimuli (the acidic pH and NTR) associated with BC tumors, demonstrating programmable response behavior, enabling highly precise and sensitive imaging of both primary BC tumors and their lung metastases. **HPNs** consist of two functional components: an ionizable diblock copolymer poly(ethylene glycol)-*b*-poly(-2-(diisopropylamino)ethyl methacrylate-*r*-2-aminoethyl methacrylate) (**PEG-*b*-(DPA-*r*-AMA)**), responsible for UPS size-switchable delivery to distinguish the acidic tumor extracellular environment (lock 1), and an NTR-activatable fluorogenic reporter **hCy-NO$_2$** incorporated inside **HPNs** for *in situ* activation under high levels of NTR (lock 2). During blood circulation, the tailored probe **HPNs** forms compact nanomicelles and keeps silent. Upon accumulation into tumor tissue through the enhanced permeability and retention (EPR) effect, **HPNs** with size-switchable properties are immediately disassembled into unimers in response to the acidic extracellular pH of tumors, leading to effective exposure of caged reporter **hCy-NO$_2$**. The resulting dissociated unimers are preferentially internalized, facilitating deep penetration into solid BC tumors and lung

https://doi.org/10.1021/jacsau.4c00356
JACS Au 2024, 4, 2606−2616

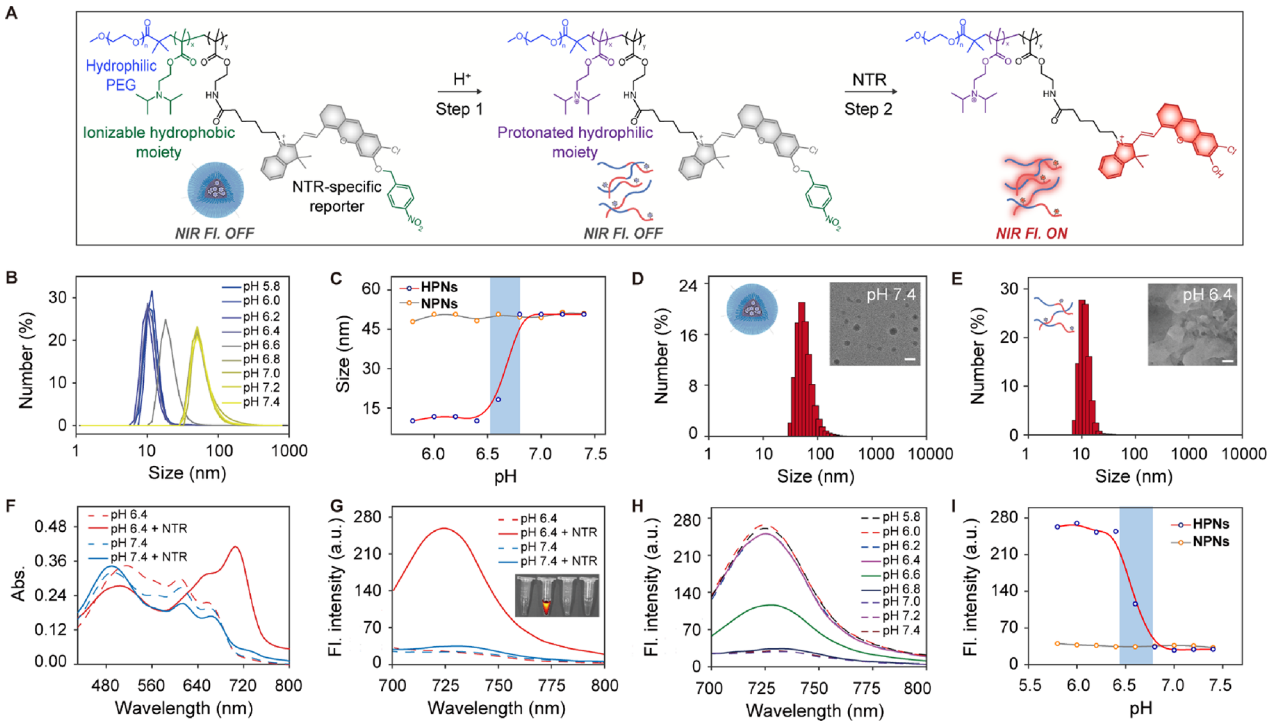

Figure 1. (A) Chemical structure and the responsive progress of pH-mediated size and fluorescent switchable behavior of cascade-activatable nanoprobes. (B) DLS distribution of **HPNs** in different pH conditions. (C) pH-dependent size properties of **HPNs** and **NPNs**. Hydrodynamic diameters and TEM images of **HPNs** at pH 7.4 (D) and pH 6.4 (E), scale bar = 100 μm. (F) Absorption and (G) fluorescence of **HPNs** (10 $\mu g \cdot mL^{-1}$) toward NTR (14 $\mu g \cdot mL^{-1}$) in PBS buffer at pH 7.4 or 6.4 for 0.5 h at 37 °C. Inset: NIRF image of **HPNs** before and after reacting with the NTR enzyme. Ex/Em = 640/725 nm. (H) Fluorescent response of **HPNs** toward NTR in different pH conditions. (I) Fluorescence intensity as a function of pH for **HPNs** and **NPNs** with addition of NTR.

metastases, subsequently generating intense fluorescence turn-on signals toward overexpressed NTR. By employing the site-specific cascade activation strategy, two specific stimuli triggers are elaborately designed to guarantee targeted accumulation at lesion sites, thereby generating enhanced fluorescence signals. Consequently, this strategy not only enables the highly precise identification of *in situ* BC but also facilitates accurate visualization of pulmonary BC metastases (Scheme 1).

RESULTS AND DISCUSSION

Preparation and Sensing Properties of HPNs

HPNs were prepared following the detailed synthetic route depicted in Scheme S2. First, an ionizable diblock copolymer **PEG-*b*-(DPA-*r*-AMA)** was prepared via atom-transfer radical polymerization (ATRP). Subsequently, an NTR-specific fluorogenic reporter **hCy-NO$_2$** was synthesized (Scheme S1) and incorporated into the copolymer **PEG-*b*-(DPA-*r*-AMA)** to afford copolymer-reporter conjugate **PEG-*b*-(DPA-*r*-hCy-NO$_2$)**. The tailored UPS nanoprobe **HPNs** were then fabricated by self-assembly of the amphiphilic **PEG-*b*-(DPA-*r*-hCy-NO$_2$)** under neutral pH conditions. The pH-insensitive polymer **PEG-*b*-(IMA-*r*-hCy-NO$_2$)** (nanoprobe **NPNs**) were synthesized by replacing the ionizable tertiary amine with a nonionizing moiety isopentyl methacrylate, and the other structural units remained consistent with **HPNs** (Scheme S2). **hCy-NO$_2$, HPNs, NPNs**, and intermediates were confirmed by ^{1}H NMR, ^{13}C NMR, and high-resolution mass spectrometry (HRMS) (Figures S21−S36).

We initially investigated the pH-dependent size-switchable behavior of **HPNs** (Figure 1A). As shown in Figure 1B, under neutral pH conditions, **HPNs** exhibited a dynamic light scattering (DLS) size of 50 nm due to the self-assembly behavior driven by the amphipathic nature of **PEG-*b*-(DPA-*r*-hCy-NO$_2$)**, resulting in the formation of nanomicelles **HPNs** in aqueous solution. Upon exposure to acidic conditions, **HPNs** dissociated into unimers with a reduced DLS size of approximately 10 nm. Notably, **HPNs** demonstrated that a narrow size switches pH (6.4−6.8), with optical pH transitions occurring at 6.6, precisely matching the extracellular tumor pH range (6.5−6.9) (Figure 1C). As expected, **HPNs** possessed an appropriate pK_a of 6.6 and exhibited remarkable sensitivity toward subtle pH changes. The morphological characteristics of **HPNs** were investigated by using transmission electron microscopy (TEM). At physiological pH, spherical morphology was observed for **HPNs** with a particle size of 52 ± 5 nm; however, significant dissociation occurred under acidic conditions (pH = 6.4) (Figure 1D,E). Meanwhile, the zeta potential (ζ) of **HPNs** was −2 mV at neutral pH but increased to 12 mV upon adjustment to a lower pH value of 6.4, indicating protonation within an acidic environment (Figures S1A and S2). These findings collectively indicate that **HPNs** are well suited for detecting subtle acidity variations between tumors and normal tissues effectively. In contrast, non-responsive nanoparticles (**NPNs**) maintained a consistent DLS size of 50 nm and had a zeta potential of −2 mV when dispersed in an aqueous solution (Figure 1C and Figure S1A). However, no significant differences were observed regarding their DLS size or zeta potential after exposure to acidic conditions (Figures S1B and S2).

The spectral responses of **HPNs** to acidic conditions and high levels of NTR were investigated. As shown in Figure

https://doi.org/10.1021/jacsau.4c00356
JACS Au 2024, 4, 2606−2616

1F,G, **HPNs** exhibited two distinct absorbance peaks at approximately 500 and 600 nm with weak fluorescence in the NIR region at pH 7.4. In the presence of NTR at pH 7.4, negligible changes were observed in the fluorescence and absorption spectra of **HPNs**. Meanwhile, despite dissociation occurring at pH 6.4, there was no substantial increase in fluorescence due to the caged states of the fluorogenic reporter. Notably, upon exposure to NTR at pH 6.4, **HPNs** exhibited an increased absorption peak at 710 nm, along with a dramatic increase in NIR fluorescence (Figure 1F,G).

Cascade-activated behaviors of **HPNs** were further investigated. Pretreatment of **HPNs** with NTR at pH 7.4 did not expedite the fluorescence increase but instead exhibited similar kinetics to both H^+ and NTR-treated **HPNs** after the addition of weak acid (pH 6.4) (Figure S3). This can be attributed to the compact encapsulation of reporter by UPS nanomicelles, which hinders the reaction and activation of fluorescence caused by high levels of NTR. Therefore, these cascade-activatable fluorogenic nanomicelles only activate NIR fluorescence when both weak acidity and NTR are present, demonstrating improved accuracy as well as excellent fidelity in fluorescence under a complex organism. In addition, NIR fluorescence images of **HPNs** with different treatments were consistent with their corresponding fluorescence spectra, highlighting their potential for tumor imaging *in vivo* (insets in Figure 1G). In contrast, nonresponsive **NPNs** displayed weak fluorescence regardless of different stimuli due to their insensitivity toward acidic fluctuations, thereby impeding disassembly and activation by NTR under both acidic and neutral conditions (Figure S4). The sensitivity of the fluorescence response of **HPNs** to subtle pH changes was further investigated. In the presence of NTR, the fluorescence intensity of **HPNs** was negligible when the pH exceeded 6.8. However, a significant increase in NIR fluorescence was observed as the pH decreased to 6.6 and complete activation occurred at pH 6.4, demonstrating distinct fluorescence activation within a narrow range of 0.4 pH units (Figure 1H,I). In contrast, nonresponsive **NPNs** exhibited no significant change in fluorescence under the same conditions (Figure S5). Furthermore, no significant changes were observed in DLS sizes even after a period of 30 days following preparation, thus manifesting the excellent colloidal stability of **HPNs** (Figure S6).

The fluorescent responsiveness of **HPNs** toward various concentrations of NTR was further investigated at pH 6.4. Upon incubation with NTR, the fluorescence intensity of **HPNs** at 725 nm exhibited a gradual increase and reached plateaus after the addition of NTR for 20 min at pH 6.4 (Figure S7). Moreover, higher concentrations of NTR led to a more pronounced enhancement of the fluorescence intensity. Consistently, as the levels of NTR increased at pH 6.4, the absorption peak of **HPNs** showed a gradual bathochromic shift from 600 to 710 nm (Figure 2A). Simultaneously, the fluorescence intensity of **HPNs** at 725 nm gradually increased with an increasing concentration of NTR, exhibiting favorable linearity within low concentrations ranging from 0 to 12 $\mu g \cdot mL^{-1}$, with a limit of detection as low as 0.024 $\mu g \cdot mL^{-1}$ (Figure 2B,C). Moreover, the selectivity evaluation revealed that only when exposed to NTR at pH 6.4 did HPNs exhibit a significant increase in NIR fluorescence. Negligible fluorescence was observed in the presence of different potential interferents, highlighting excellent specificity in complicated biosystems (Figure 2D and Figure S8). Optical stability studies

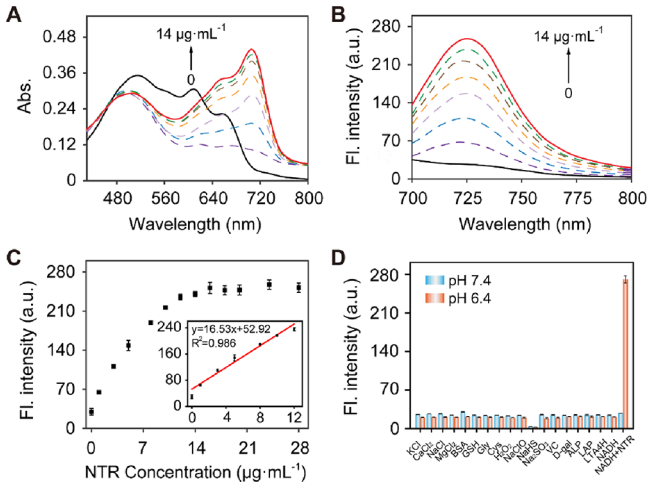

Figure 2. *In vitro* characterization of **HPNs** at pH 6.4. (A) Absorption and (B) fluorescence changes to different concentrations of NTR (0−14 $\mu g \cdot mL^{-1}$). (C) The maximum fluorescence intensity increased with increasing concentrations of NTR (0−28 $\mu g \cdot mL^{-1}$). Inset: linear fluorescence responses toward 0−12 $\mu g \cdot mL^{-1}$ of NTR. (D) Selectivity studies of **HPNs** at pH 6.4 and 7.4 solution. Ex/Em = 640/725 nm.

showed consistent fluorescence of **HPNs** under continuous irradiation, emphasizing their tremendous potential for dynamically fluorescent monitoring and imaging pathological progresses *in vivo* (Figure S9). In brief, **HPNs** exhibited excellent cascade activation toward weak acidity and specifically targeted NTR, which are crucial for achieving high SBR imaging *in vivo* and precise identification of tiny tumors from normal tissues.

Cellular Uptake Imaging

To further evaluate the fluorescence imaging capability of **HPNs** in 4T1 and A549 cells, we proceeded to investigate the cascade-activatable fluorogenic response. First, the biosafety of **HPNs** and **NPNs** was evaluated. The viability of 4T1 and A549 cells remained above 80% even at a concentration of 10 $\mu g \cdot mL^{-1}$ probes, demonstrating their good biocompatibility (Figure S10). Next, acid pH and NTR orthotropic fluorescence imaging was studied in cells. To induce various levels of endogenous NTR expression, cells were preincubated under hypoxic conditions (1% hypoxia, 5% microanoxia, and 21% normoxia) (Figure 3A). As shown in Figure 3B, treatment of 4T1 cells with **HPNs** resulted in negligible fluorescence at pH 6.4 under normoxia conditions due to the relatively low expression level of endogenous NTR in normal state 4T1 cells. In addition, cellular fluorescence gradually increased within the treated 4T1 cells as the oxygen content decreased at pH 6.4, which was five times higher than that observed under normoxic conditions (Figure 3C). Cobalt ion (Co^{2+}) has been proved to induce microanoxia condition (about 8% O_2), which also led to a slight increase fluorescence intensity. Furthermore, negligible fluorescence was observed in **HPNs**-treated 4T1 cells subjected to neutral incubation under hypoxic conditions due to the restricted nanostructure hindering further activation of the internal fluorogenic reporter by NTR. As anticipated, only when exposed to both hypoxia and slightly acidic treatment did **HPNs** exhibit activated fluorescence in 4T1 cells. Moreover, an inhibitory study using dicoumarol (Dic) as an inhibitor of NTR was conducted. The fluorescence signal of **HPNs** from Dic-pretreated 4T1 cells was significantly suppressed upon incubation under hypoxic conditions at pH

https://doi.org/10.1021/jacsau.4c00356
JACS Au 2024, 4, 2606−2616

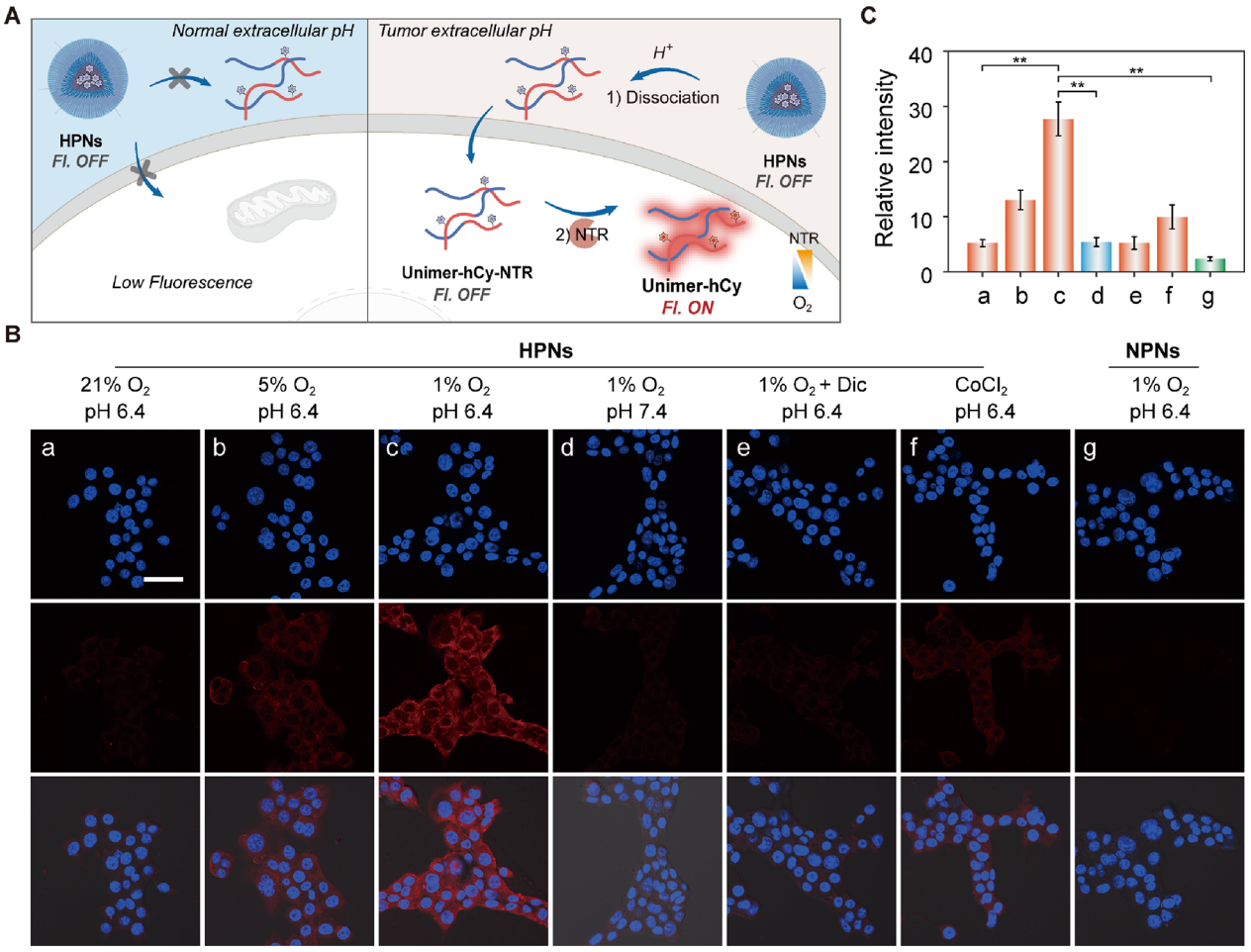

Figure 3. (A) Cartoon illustration and (B) confocal fluorescence imaging of 4T1 cells incubated with **HPNs** or **NPNs** (10 μg·mL^{-1}) under different conditions. a: **HPNs** in pH 6.4 under normoxic (21% O_2) condition; b: **HPNs** in pH 6.4 under microaerobic (5% O_2) condition; c: **HPNs** in pH 6.4 under hypoxic (1% O_2) condition; d: **HPNs** in pH 7.4 under hypoxic (1% O_2) condition; e: **HPNs** + inhibitor Dic in pH 6.4 under hypoxic (1% O_2) condition; f: **HPNs** + $CoCl_2$ in pH 6.4; g: **NPNs** in pH 6.4 under hypoxic (1% O_2) condition. (C) Relative quantitative analysis of the corresponding fluorescence intensity in (B). Scale bar: 25 μm. *P < 0.05, **P < 0.01, and ***P < 0.001.

6.4, demonstrating effective inhibition by Dic and highlighting the high selectivity of **HPNs** to NTR (Figure 3B). Therefore, the synergistic stimulation of the tumor acidic environment and NTR ensures specific imaging and accurate detection in BC cells. In contrast, 4T1 cells treated with **NPNs** showed a negligible increase in fluorescence after hypoxic incubation at an acidic pH, consistent with their insensitivity toward pH fluctuations *in vitro* (Figure 3B). Fluorescence images obtained from A549 cells treated with **HPNs** displayed similar trends in fluorescence signals as those observed in 4T1 cells (Figure S11). Moreover, cellular fluorescence images obtained from **HPNs-hCy**-treated 4T1 and A549 cells at pH 6.4 exhibited distinct red fluorescence under both hypoxic and normoxic conditions (Figure S12). Conversely, under hypoxic conditions, the treatment of cells with **HPNs-hCy** resulted in relatively negligible fluorescence at pH 7.4, further highlighting the superiority of the cascade-activated strategy. Therefore, **HPNs** enable precise fluorescence imaging for the synergetic detection of solid tumor-specific slight acidity and hypoxia conditions, making them suitable for overcoming false-positive signals encountered by single-activatable probes and achieving precise tumor imaging.

It is speculated that the protonation and dissociation of **HPNs** into small-sized unimers at acidic pH facilitate their cellular internalization, thereby accelerating intracellular activation by NTR. To further validate this hypothesis, always-on nanomicells **Ol-PNs** were prepared using an uncaged hCy reporter under optimized conditions. As shown in Figure S13, intense fluorescence was observed on the cytomembrane of 4T1 cells after incubation with **Ol-PNs** for 0.5 h. The fluorescence signal gradually increased within 4T1 cells at pH 6.4, proving the internalization of unimers of **Ol-PNs** by 4T1 cells. However, even after 2 h of treatment with **Ol-PNs** at neutral pH, the fluorescence remained localized on the cytomembrane of 4T1 cells. Consistent with expectations, the protonation and dissociation of nanomicells into positively charged unimers under acid condition enable their rapid cellular uptake and facilitate efficient imaging of relevant tumors.[43,44]

Penetration in 4T1 Tumor Spheroids

Inspired by the rapid internalization of proposed nanomicells under acidic pH, we suggested that the protonation and dissociation of **HPNs** may facilitate their uptake into solid tumors. To evaluate the penetrability of **HPNs**, a three-dimensional multicellular spheroid (4T1 tumor spheroid) was cultured under hypoxic conditions to mimic the morphology and biological microenvironment of solid tumors (Figure 4).

https://doi.org/10.1021/jacsau.4c00356
JACS Au 2024, 4, 2606−2616

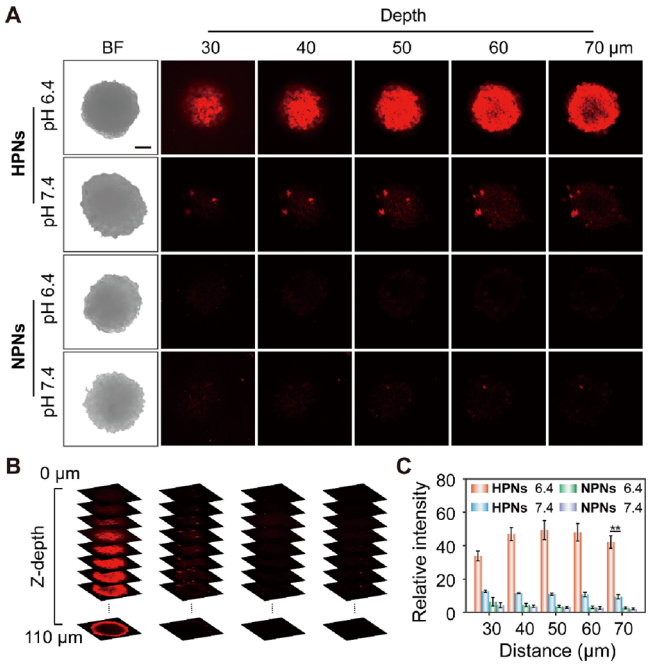

Figure 4. Permeability profile of **HPNs** and **NPNs**. (A) and (B) *Z*-stack scanning of 4T1 tumor spheroids treated with **HPNs** and **NPNs** at pH 7.4 or 6.4 for 8 h. (C) Semiquantitative fluorescence analysis in (A) in the *Z*-stack scanning distance. Scale bar: 100 μm. *P < 0.05, **P < 0.01, and ***P < 0.001.

Upon incubation with **HPNs** at pH 7.4, slight fluorescence was observed in the peripheral region of the 4T1 tumor spheroid (Figure 4A). Surprisingly, upon treatment with **HPNs** at pH 6.4, significant fluorescence was detected within the tumor spheroid. *Z*-stack scanning fluorescence images revealed that even at a depth of 60 μm inside the tumor spheroid, the fluorescence signal remained strong, exhibiting over a three-fold higher intensity compared to that observed in **HPNs**-treated tumor spheroid at pH 7.4, proving remarkable penetration capability of small-sized unimers (Figure 4B,C). In contrast, negligible fluorescence was observed in **NPNs**-treated tumor spheroids at both neutral and acidic pH due to limited penetration caused by their large size (Figure 4A,B). Therefore, through its size-switchable property, UPS nanoprobe **HPNs** effectively enhance penetration into interior regions of tumors as well as specific activation by high levels of NTR, further achieving sensitive and accurate imaging for solid tumors. This finding encourages further investigation into its promising potential for detecting BC and lung metastasis through *in vivo* imaging.

In Vivo Imaging of 4T1 Tumor-Bearing Mice

Inspired by the effective penetrability and cascade responsiveness of **HPNs** *in vitro*, our subsequent focus shifted to evaluating the *in vivo* imaging performance of **HPNs**. The nanoscale size and PEGylation of **HPNs** enable prolonged circulation in the bloodstream and improved passive accumulation in solid tumors through the EPR effect. First, the tumor accumulation and imaging performance of **HPNs**

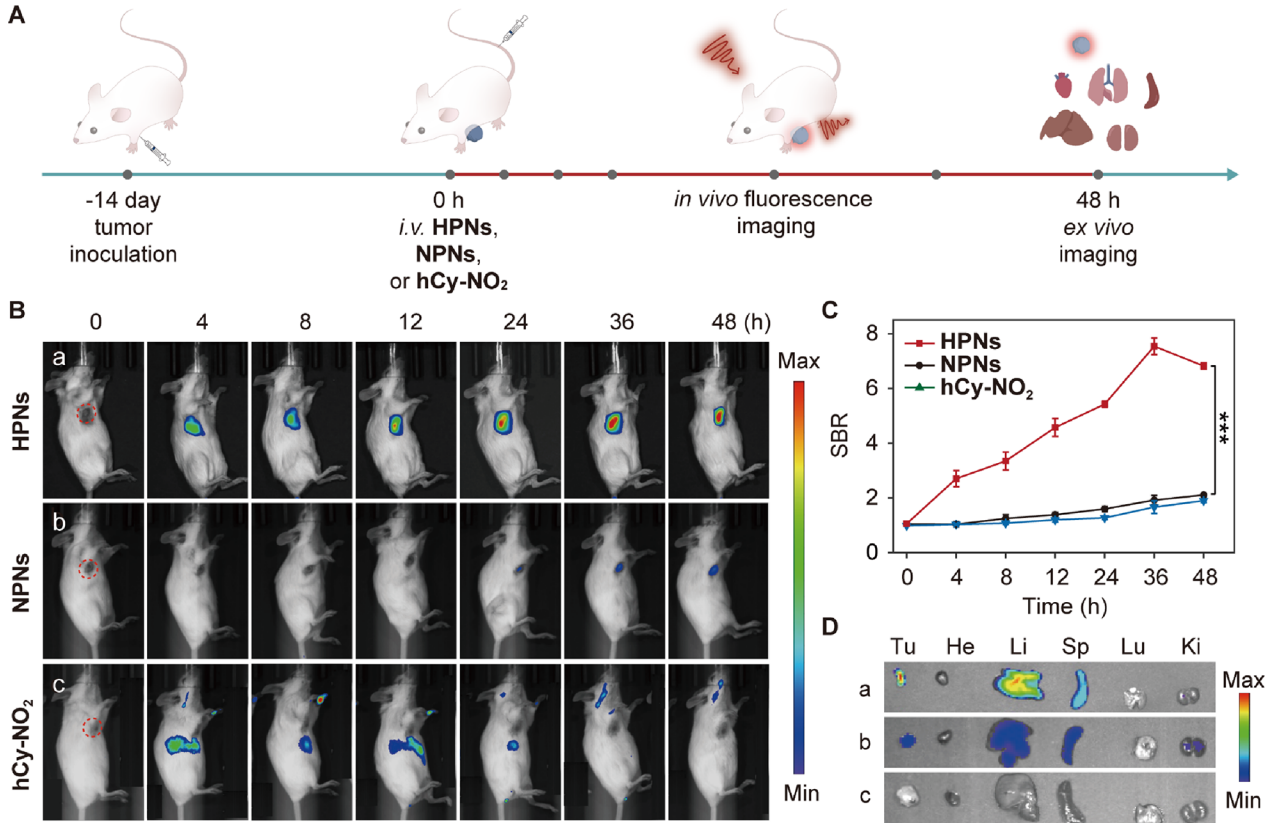

Figure 5. Fluorescence tracking of the programmable stimulus activation in a 4T1 subcutaneous xenografted tumor model. (A) Timeline for the construction of implantation of 4T1 tumor-bearing mice and time-dependent imaging. (B) *In vivo* fluorescence imaging of different treatment groups. a: **HPNs**; b: **NPNs**; c: **hCy-NO$_2$**. Red circles: the tumor region. (C) Quantification of fluorescence intensities in (B). (D) *Ex vivo* imaging of different treatment groups after 48 h. Ex/Em = 675/740 nm. *P < 0.05, **P < 0.01, and ***P < 0.001.

https://doi.org/10.1021/jacsau.4c00356
JACS Au 2024, 4, 2606−2616

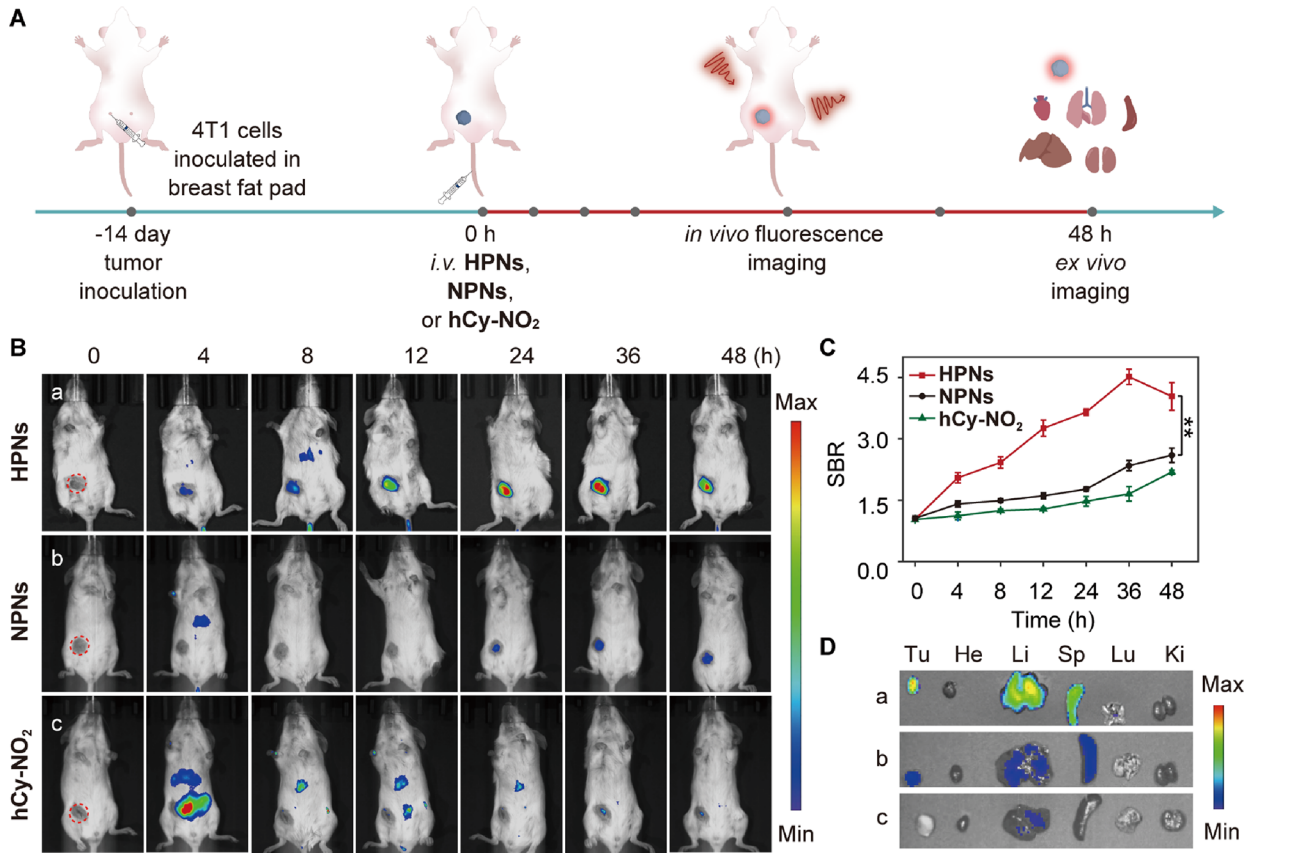

Figure 6. Fluorescence tracking of the programmable stimulus activation in the primary 4T1 BC cancer model. (A) Timeline for the construction of implantation of primary 4T1 tumor-bearing mice and time-dependent imaging. (B) *In vivo* fluorescence imaging of different treatment groups. a: **HPNs**; b: **NPNs**; c: **hCy-NO$_2$**. Red circles: the tumor region. (C) Quantification of fluorescence intensities in (B). (D) *Ex vivo* imaging of different treatment groups after 48 h. Ex/Em = 675/740 nm. *P < 0.05, **P < 0.01, and ***P < 0.001.

were investigated in a 4T1 subcutaneous xenografted tumor model (Figure 5A). As shown in Figure 5B, specific fluorescence was observed exclusively within the tumor regions following intravenous (*i.v.*) injection of **HPNs**, with the fluorescence signal gradually increasing over time until reaching the maximum at 36 h postinjection. Meanwhile, negligible fluorescence was observed outside of these regions due to both the EPR effect and the cascade-activated behaviors of **HPNs**, highlighting their superiority in effectively reducing background signal and identifying BC tumors. In contrast, mice treated with **NPNs** displayed significantly weaker fluorescence signals within the tumor regions, consistent with the results of *in vitro* studies. Additionally, mice were pretreated intratumorally (*i.t.*) with $NaHCO_3$ or Dic to individually modulate the acidity or NTR activity within tumor tissues. As anticipated, both groups showed substantial suppression of fluorescence signals (Figure S14). Furthermore, no obvious fluorescence was observed within the tumor regions following *i.v.* injection of small-molecule reporter **hCy-NO$_2$**, due to its limited accumulation in tumors and rapid clearance from the liver. Notably, compared with **hCy-NO$_2$** at all monitoring times, **HPNs** showed significantly higher levels of accumulation within tumor tissues. The fluorescence quantitation revealed that NIR fluorescence in the tumor regions of mice treated with **HPNs** was four times higher than that of mice treated with other substances at 36 h postinjection. This finding highlights the advantageous cascade-activated behaviors of **HPNs**, enabling the highly sensitive detection and precise imaging of BC tumors (Figure 5C). At 48 h postinjection, the mice were euthanized for subsequent *ex vivo* fluorescence imaging of major organs and tumors. In line with the findings from *in vivo* imaging, there was a substantial increase in NIR fluorescence in tumors from the mice treated with **HPNs** compared to other groups (Figure 5D). In conclusion, **HPNs** serve as cascade-activated nanomicells that maintain nonfluorescence during blood circulation but exhibit specific fluorescence signals for highly accurate diagnosis of BC tumors.

HPNs were further utilized for imaging an orthotopic BC model *in vivo*, which provided a more realistic BC microenvironment (Figure 6A). As illustrated in Figure 6B,C, upon *i.v.* injection of **HPNs**, the orthotopic 4T1 tumor exhibited bright fluorescence at 4 h postinjection. The fluorescence was persistently enhanced over time and reached a maximum approximately two times higher than that of the control group at 36 h, indicating effective imaging performance in an orthotopic 4T1 tumor with a high SBR (Figure 6C). In comparison, weak fluorescence signals were observed in the tumor regions of **NPNs**-treated mice during 24 h postinjection. Nonspecific activation and fast hepato-enteric metabolism of small-molecule single-activatable **hCy-NO$_2$** failed to achieve high-contrast imaging of orthotopic BC tumors (Figure 6B). In addition, weak fluorescence was observed in $NaHCO_3$ and Dic-pretreated mice, demonstrating that nanomicells **HPNs** maintained silent in tumors due to unfinished cascade behavior (Figure S15). Further investigation into imaging effects on

https://doi.org/10.1021/jacsau.4c00356
JACS Au 2024, 4, 2606−2616

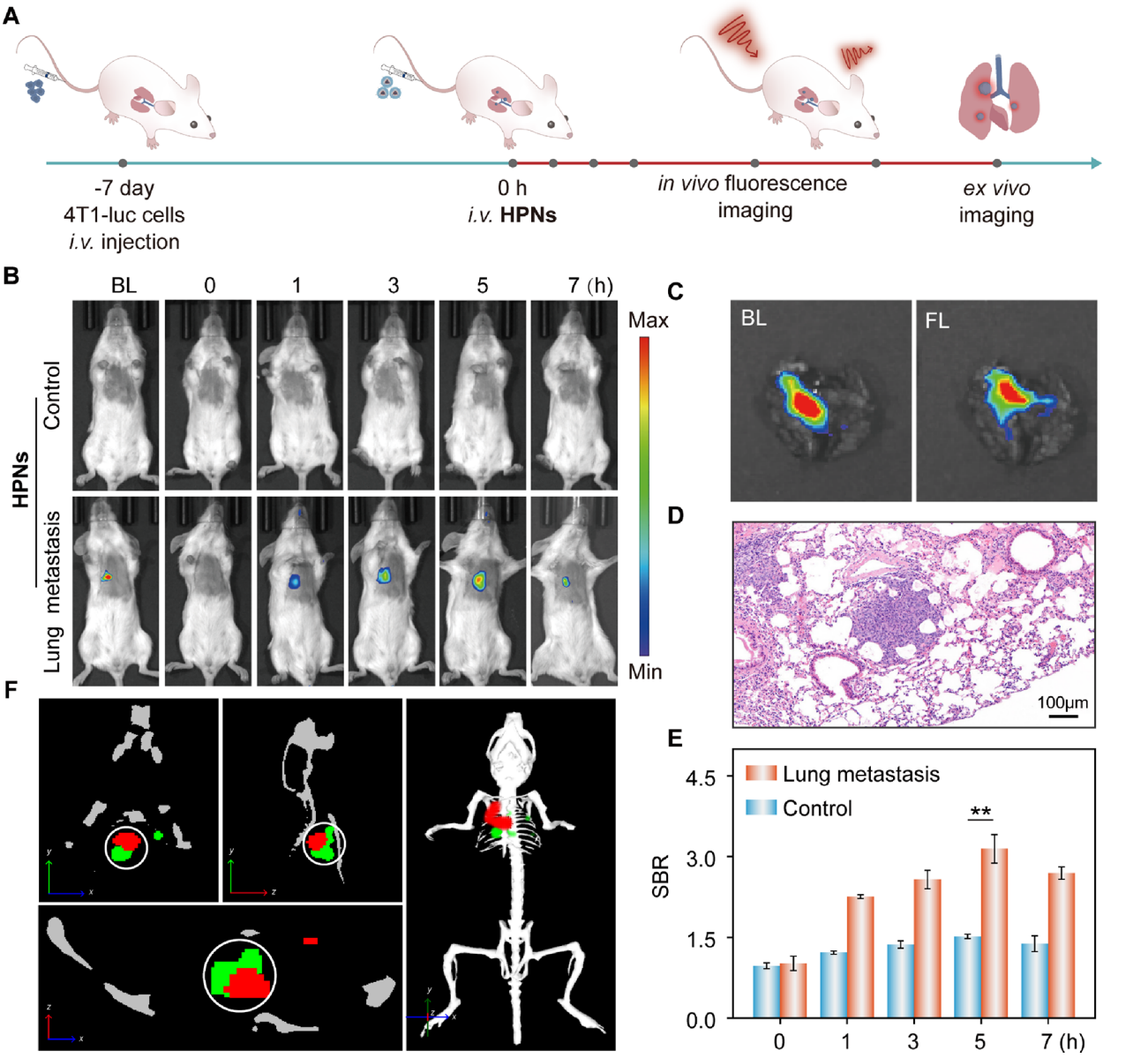

Figure 7. Fluorescence tracking of the programmable stimulus activation in lung metastatic breast cancer model. (A) Timeline for the construction of implantation of lung metastasis-bearing mice and time-dependent imaging. (B) *In vivo* fluorescence imaging of different treatment groups. (C) *Ex vivo* bioluminescence and fluorescence images and (D) H&E analysis of the dissected metastatic tumor tissues. (E) Quantification of fluorescence intensities in (B). Ex/Em = 675/740 nm. (F) The reconstructed three-dimensional (3D) images of lung metastasis-bearing mice. The green signals: bioluminescence signal; the red signals: fluorescence signal. $^{*}P < 0.05$, $^{**}P < 0.01$, and $^{***}P < 0.001$.

orthotopic BC tumors confirmed high accumulation and specific fluorescence activation through captured *ex vivo* images (Figure 6D). Therefore, the eminent performance of **HPNs** mainly benefited from the cascade ultrasensitive pH response and NTR activation capabilities, ensuring low background signal and high SBR at 4T1 orthotopic tumors. Clearly, this intelligent scenario can be achieved through the combined utility of size-switchable delivery in the tumor microenvironment, efficient intracellular internalization, and programmable NTR-specific activation strategy in the site-specific cascade-activation design, which holds promising potential for achieving high-contrast and precise imaging in a 4T1 orthotopic tumor model.

In Vivo Investigation of the Lung Metastatic Breast Cancer Model for HPNs

Accurate detection of tiny peritoneal lung metastases is crucial for the early diagnosis and timely treatment of BC. Inspired by the superior *in situ* imaging performance of proposed nanomicelles **HPNs** in a primary BC model, we further investigated their specific precision imaging capabilities in a BC lung metastatic mouse model established by *i.v.* injection of 4T1-luciferase cells (Figure 7A). Bioluminescence (BL) imaging was initially performed to monitor the presence and location of lung metastases. Healthy mice were used as the control group. Both healthy mice and mice bearing lung metastasis were administered **HPNs** via tail vein injection. As shown in Figure 7B, the NIR fluorescence image clearly illuminated occult metastases focus, accurately pinpointing

https://doi.org/10.1021/jacsau.4c00356
JACS Au 2024, 4, 2606−2616

their locations that corresponded to BL signals observed *in vivo* from tumor metastases. This exceptional performance highlights the ability of cascade-activatable fluorogenic nanomicelles **HPNs** to identify sites of metastasis. Furthermore, NIR fluorescence gradually increased over time and reached considerable brightness at 7 h within the lung region; conversely, a negligible fluorescence signal was observed in healthy mice (Figure 7B). Additionally, *ex vivo* imaging of harvested lung tissues from mice bearing lung metastasis revealed precise localization through overlapping of the BL and fluorescence signals from **HPNs** (Figure 7C). Histological morphology (H&E staining) further confirmed that these signals corresponded to tumor nodules (Figure 7D). Immunohistochemical staining with HIF-α and MCT-4 revealed that the metastasis foci exhibited higher levels of hypoxia and acidity compared to the adjacent normal lung tissue, thereby indicating pH and NTR cascade activation of **HPNs** toward lung metastases foci (Figure S16). Therefore, **HPNs** facilitated clear visualization of lung metastatic nodules with minimal background signals, thus showcasing their exceptional ability to distinguish metastatic sites from adjacent normal tissues. Quantitative analysis revealed a two-fold increase in lung fluorescence intensity in BC lung metastasis mice compared to healthy mice at 5 h, illustrating the efficacy of **HPNs** for detecting lung metastases (Figure 7E). These results convincingly proved that due to effective programmable stimulus activation within an acidic tumor environment and overexpressed NTR, **HPNs** hold significant potential for achieving remarkable SBR imaging and accurate diagnosis of lung metastases *in vivo*.

The reconstructed three-dimensional (3D) images were acquired to investigate the specific targeting imaging of **HPNs** toward lung metastatic foci by the IVIS Spectrum imaging system. Co-localization analysis was performed on the NIR fluorescence signals emitted by **HPNs** (red), the BL signals emitted by 4T1-uc tumors (green) in metastatic nodules and anatomical profiles of mice to evaluate the performance of specific metastasis targeting imaging (Figure 7F and Figure S17). Remarkably, *in vivo* multi-channel imaging profiles readily detected red fluorescence signals at metastatic sites in the lung tissues, which exhibited a significant overlap with BL signals from metastatic nodules (white circle), indicating a specific and efficient targeting of **HPNs** toward pulmonary metastasis. These observations were also clearly discernible in the reconstructed 3D movies. In addition, H&E staining, hemolysis analysis, and body weight measurement showed no significant physiological abnormalities under different treated mice, demonstrating the biosafety of **HPNs** for *in vivo* imaging applications (Figures S18−S20). These results strongly demonstrate site-specific activation and effective targeting of **HPNs** toward metastatic nodules, enabling real-time tracking of pulmonary metastasis.

CONCLUSIONS

In summary, we have developed a cascade activation strategy for real-time tracking of orthotopic BC and pulmonary metastasis. By loading NTR-activated fluorogenic reporters in UPS block copolymers, we successfully designed a site-specific cascade-activatable NIR fluorogenic nanoprobe **HPNs**. Due to the ultrasensitive pH response features, **HPNs** transform into unimers within the acidic tumor microenvironment and exhibit significant fluorescence upon high levels of NTR activation, enabling accurate identification of BC lung metastasis. More importantly, the cascade activation strategy ensures that **HPNs** remain inactive in the blood circulation and healthy tissues, effectively reducing the background signal and significantly improving the fidelity of the fluorescent signal. The programmable activation ability of **HPNs** effectively addresses the issue of low accuracy and reliability associated with the single-stimulus strategy, thereby achieving ultrahigh SBR imaging and precise diagnosis of orthotopic BC tumors as well as their lung metastatic foci *in vivo*. These efforts not only provide a potential platform for accurate diagnosis of BC tumors and lung metastases but also offer a promising strategy for scaling up construction of superior probes to identify elusive lesions and facilitate therapy.

ASSOCIATED CONTENT

Supporting Information

The Supporting Information is available free of charge at https://pubs.acs.org/doi/10.1021/jacsau.4c00356.

Additional experimental details including the materials, methods, synthetic procedures, characterization data (NMR, HRMS, etc.), ζ potential, photostability, fluorescence spectra and hydrodynamic diameter of HPNs and NPNs, *in vivo* fluorescence imaging, and additional data and figures (PDF)

Rotation video of a 3D reconstruction of bioluminescence images of lung metastasis-bearing mice (AVI)

Rotation video of a 3D reconstruction of fluorescence images of lung metastasis-bearing mice (AVI)

AUTHOR INFORMATION

Corresponding Authors

Xueyun Gao − *Center of Excellence for Environmental Safety and Biological Effects, Beijing Key Laboratory for Green Catalysis and Separation, Department of Chemistry, Beijing University of Technology, Beijing 100124, P. R. China;* orcid.org/0000-0002-2267-9945; Email: gaoxy@ihep.ac.cn

Dongdong Su − *Center of Excellence for Environmental Safety and Biological Effects, Beijing Key Laboratory for Green Catalysis and Separation, Department of Chemistry, Beijing University of Technology, Beijing 100124, P. R. China;* orcid.org/0000-0002-7463-4466; Email: chmsudd@bjut.edu.cn

Authors

Xueqian Chen − *Center of Excellence for Environmental Safety and Biological Effects, Beijing Key Laboratory for Green Catalysis and Separation, Department of Chemistry, Beijing University of Technology, Beijing 100124, P. R. China*

Jiatian Liu − *Center of Excellence for Environmental Safety and Biological Effects, Beijing Key Laboratory for Green Catalysis and Separation, Department of Chemistry, Beijing University of Technology, Beijing 100124, P. R. China*

Yong Zhang − *Center of Excellence for Environmental Safety and Biological Effects, Beijing Key Laboratory for Green Catalysis and Separation, Department of Chemistry, Beijing University of Technology, Beijing 100124, P. R. China*

Complete contact information is available at: https://pubs.acs.org/10.1021/jacsau.4c00356

Author Contributions

X.C. conceived and performed the experimental work and wrote the first draft of the manuscript. J.L. and Y.Z. carried out practical work and discussed the results. X.G. and D.S. supervised the work, discussed experiments and results, and wrote the final manuscript. All authors have approved the final version of the manuscript.

Notes

The authors declare no competing financial interest.

■ ACKNOWLEDGMENTS

The authors acknowledge support from the National Key Research & Development Program of China (grant nos. 2021YFA1201000, 2022YFA1207300), the National Natural Science Foundation of China (nos. 22274005, 22334001, U2067214, U2167222, 32171378), and the Beijing Outstanding Young Scientist Program (No. BJJWZYJH01201910005017).

■ ABBREVIATIONS

BC, breast cancer; UPS, ultra-pH-sensitive; SBR, signal-to-background ratio; DLS, dynamic light scattering; NTR, nitroreductase; H&E, hematoxylin and eosin; NIR, near-infrared; PEG, polyethylene glycol.

■ REFERENCES

(1) Massague, J.; Obenauf, A. C. Metastatic colonization by circulating tumour cells. *Nature* **2016**, *529*, 298−306.
(2) Cao, H.; Wang, H.; He, X.; Tan, T.; Hu, H.; Wang, Z.; Wang, J.; Li, J.; Zhang, Z.; Li, Y. Bioengineered Macrophages Can Responsively Transform into Nanovesicles To Target Lung Metastasis. *Nano Lett.* **2018**, *18*, 4762−4770.
(3) Barzaman, K.; Karami, J.; Zarei, Z.; Hosseinzadeh, A.; Kazemi, M. H.; Moradi-Kalbolandi, S.; Safari, E.; Farahmand, L. Breast cancer: Biology, biomarkers, and treatments. *Int. Immunopharmacol.* **2020**, *84*, No. 106535.
(4) Jia, Q.; Li, Z.; Bai, M.; Yan, H.; Zhang, R.; Ji, Y.; Feng, Y.; Yang, Z.; Wang, Z.; Li, J. Estimating dynamic vascular perfusion based on Er-based lanthanide nanoprobes with enhanced down-conversion emission beyond 1500 nm. *Theranostics* **2021**, *11*, 9859−9872.
(5) Terao, M.; Niikura, N. Diagnosis of oligometastasis. *Transl. Cancer Res.* **2020**, *9*, 5032−5037.
(6) Jia, Q.; Zhang, R.; Yan, H.; Feng, Y.; Sun, F.; Yang, Z.; Qiao, C.; Mou, X.; Tian, J.; Wang, Z. An Activatable Near-Infrared Fluorescent Probe for Precise Detection of the Pulmonary Metastatic Tumors: A Traditional Molecule Having a Stunning Turn. *Angew. Chem.* **2023**, *62*, No. e202313420.
(7) Gerull, W. D.; Puri, V.; Kozower, B. D. The epidemiology and biology of pulmonary metastases. *J. Thorac. Dis.* **2021**, *13*, 2585−2589.
(8) Eckerling, A.; Ricon-Becker, I.; Sorski, L.; Sandbank, E.; Ben-Eliyahu, S. Stress and cancer: mechanisms, significance and future directions. *Nat. Rev. Cancer* **2021**, *21*, 767−785.
(9) Esposito, M.; Ganesan, S.; Kang, Y. Emerging strategies for treating metastasis. *Nat. Cancer* **2021**, *2*, 258−270.
(10) Hegde, M.; Naliyadhara, N.; Unnikrishnan, J.; Alqahtani, M. S.; Abbas, M.; Girisa, S.; Sethi, G.; Kunnumakkara, A. B. Nanoparticles in the diagnosis and treatment of cancer metastases: Current and future perspectives. *Cancer Lett.* **2023**, *556*, No. 216066.
(11) Zhao, H.; Liu, C.; Gu, Z.; Dong, L.; Li, F.; Yao, C.; Yang, D. Persistent Luminescent Nanoparticles Containing Hydrogels for Targeted, Sustained, and Autofluorescence-Free Tumor Metastasis Imaging. *Nano Lett.* **2020**, *20*, 252−260.
(12) Crosby, D.; Bhatia, S.; Brindle, K. M.; Coussens, L. M.; Dive, C.; Emberton, M.; Esener, S.; Fitzgerald, R. C.; Gambhir, S. S.; Kuhn, P.; Rebbeck, T. R.; Balasubramanian, S. Early detection of cancer. *Science* **2022**, *375*, No. eaay9040.
(13) Kranenburg, O.; van der Speeten, K.; de Hingh, I. Peritoneal Metastases From Colorectal Cancer: Defining and Addressing the Challenges. *Front. Oncol.* **2021**, *11*, No. 650098.
(14) Dou, W. T.; Han, H. H.; Sedgwick, A. C.; Zhu, G. B.; Zang, Y.; Yang, X. R.; Yoon, J.; James, T. D.; Li, J.; He, X. P. Fluorescent probes for the detection of disease-associated biomarkers. *Sci. Bull.* **2022**, *67*, 853−878.
(15) Li, H.; Kim, H.; Xu, F.; Han, J.; Yao, Q.; Wang, J.; Pu, K.; Peng, X.; Yoon, J. Activity-based NIR fluorescent probes based on the versatile hemicyanine scaffold: design strategy, biomedical applications, and outlook. *Chem. Soc. Rev.* **2022**, *51*, 1795−1835.
(16) Zhang, Y.; Zhang, G.; Zeng, Z.; Pu, K. Activatable molecular probes for fluorescence-guided surgery, endoscopy and tissue biopsy. *Chem. Soc. Rev.* **2022**, *51*, 566−593.
(17) Zhang, Y.; Chen, X.; Yuan, Q.; Bian, Y.; Li, M.; Wang, Y.; Gao, X.; Su, D. Enzyme-activated near-infrared fluorogenic probe with high-efficiency intrahepatic targeting ability for visualization of drug-induced liver injury. *Chem. Sci.* **2021**, *12*, 14855−14862.
(18) Zhang, Y.; Li, W.; Chen, X.; Xiong, S.; Bian, Y.; Yuan, L.; Gao, X.; Su, D. Liver-Targeted Near-Infrared Fluorescence/Photoacoustic Dual-Modal Probe for Real-Time Imaging of In Situ Hepatic Inflammation. *Anal. Chem.* **2023**, *95*, 2579−2587.
(19) Wu, L.; Huang, J.; Pu, K.; James, T. D. Dual-locked spectroscopic probes for sensing and therapy. *Nat. Rev. Chem.* **2017**, *1*, 406−421.
(20) Zheng, X.; Mao, H.; Huo, D.; Wu, W.; Liu, B.; Jiang, X. Successively activatable ultrasensitive probe for imaging tumour acidity and hypoxia. *Nat. Biomed. Eng.* **2017**, *1*, 0057.
(21) Ma, Y.; Shang, J.; Liu, L.; Li, M.; Xu, X.; Cao, H.; Xu, L.; Sun, W.; Song, G.; Zhang, X.-B. Rational Design of a Double-Locked Photoacoustic Probe for Precise In Vivo Imaging of Cathepsin B in Atherosclerotic Plaques. *J. Am. Chem. Soc.* **2023**, *145*, 17881−17891.
(22) Ma, Y.; Sun, W.; Ye, Z.; Liu, L.; Li, M.; Shang, J.; Xu, X.; Cao, H.; Xu, L.; Liu, Y.; Kong, X.; Song, G.; Zhang, X.-B. Oxidative stress biomarker triggered multiplexed tool for auxiliary diagnosis of atherosclerosis. *Sci. Adv.* **2023**, *9*, No. eadh1037.
(23) Zong, Q.; Zheng, R.; Xiao, X.; Jiang, M.; Li, J.; Yuan, Y. Dual-locking nanoprobe based on hemicyanine for orthogonal stimuli-triggered precise cancer imaging and therapy. *J. Controlled Release* **2021**, *338*, 307−315.
(24) Yan, C.; Guo, Z.; Liu, Y.; Shi, P.; Tian, H.; Zhu, W. H. A sequence-activated AND logic dual-channel fluorescent probe for tracking programmable drug release. *Chem. Sci.* **2018**, *9*, 6176−6182.
(25) Zhao, X.; Yang, C.-X.; Chen, L.-G.; Yan, X.-P. Dual-stimuli responsive and reversibly activatable theranostic nanoprobe for precision tumor-targeting and fluorescence-guided photothermal therapy. *Nat. Commun.* **2017**, *8*, 14998.
(26) Yang, G.; Phua, S. Z. F.; Lim, W. Q.; Zhang, R.; Feng, L.; Liu, G.; Wu, H.; Bindra, A. K.; Jana, D.; Liu, Z.; Zhao, Y. A Hypoxia-Responsive Albumin-Based Nanosystem for Deep Tumor Penetration and Excellent Therapeutic Efficacy. *Adv. Mater.* **2019**, *31*, No. e1901513.
(27) Wang, Y.; Shi, L.; Wu, W.; Qi, G.; Zhu, X.; Liu, B. Tumor-Activated Photosensitization and Size Transformation of Nanodrugs. *Adv. Funct. Mater.* **2021**, *31*, 2010241.
(28) Li, X.; Park, E. Y.; Kang, Y.; Kwon, N.; Yang, M.; Lee, S.; Kim, W. J.; Kim, C.; Yoon, J. Supramolecular Phthalocyanine Assemblies for Improved Photoacoustic Imaging and Photothermal Therapy. *Angew. Chem., Int. Ed. Engl.* **2020**, *59*, 8630−8634.
(29) Lin, X.; Liu, C.; Sheng, Z.; Gong, X.; Song, L.; Zhang, R.; Zheng, H.; Sun, M. Highly Sensitive Fluorescence and Photoacoustic Detection of Metastatic Breast Cancer in Mice Using Dual-Modal Nanoprobes. *ACS Appl. Mater. Interfaces* **2018**, *10*, 26064−26074.
(30) Xu, H.; Yuan, L.; Shi, Q.; Tian, Y.; Hu, F. Ultrabright NIR-II Nanoprobe for Image-Guided Accurate Resection of Tiny Metastatic Lesions. *Nano Lett.* **2024**, *24*, 1367−1375.

https://doi.org/10.1021/jacsau.4c00356
JACS Au 2024, 4, 2606−2616

(31) Zhang, Z.; Wang, Q.; Liu, Q.; Zheng, Y.; Zheng, C.; Yi, K.; Zhao, Y.; Gu, Y.; Wang, Y.; Wang, C.; Zhao, X.; Shi, L.; Kang, C.; Liu, Y. Dual-Locking Nanoparticles Disrupt the PD-1/PD-L1 Pathway for Efficient Cancer Immunotherapy. *Adv. Mater.* **2019**, *31*, No. e1905751.
(32) Bertoni, S.; Liu, Z.; Correia, A.; Martins, J. P.; Rahikkala, A.; Fontana, F.; Kemell, M.; Liu, D.; Albertini, B.; Passerini, N.; Li, W.; Santos, H. A. pH and Reactive Oxygen Species-Sequential Responsive Nano-in-Micro Composite for Targeted Therapy of Inflammatory Bowel Disease. *Adv. Funct. Mater.* **2018**, *28*, 1806175.
(33) Liu, C.; Zhang, R.; Zhang, W.; Liu, J.; Wang, Y. L.; Du, Z.; Song, B.; Xu, Z. P.; Yuan, J. "Dual-Key-and-Lock" Ruthenium Complex Probe for Lysosomal Formaldehyde in Cancer Cells and Tumors. *J. Am. Chem. Soc.* **2019**, *141*, 8462−8472.
(34) Shen, J.; Ma, M.; Shafiq, M.; Yu, H.; Lan, Z.; Chen, H. Microfluidics-Assisted Engineering of pH/Enzyme Dual-Activatable ZIF@Polymer Nanosystem for Co-Delivery of Proteins and Chemotherapeutics with Enhanced Deep-Tumor Penetration. *Angew. Chem., Int. Ed.* **2022**, *61*, No. e202113703.
(35) Xue, X.; Qu, H.; Li, Y. Stimuli-responsive crosslinked nanomedicine for cancer treatment. *Exploration* **2022**, *2*, 20210134.
(36) Chen, Y.; Ai, K.; Liu, J.; Sun, G.; Yin, Q.; Lu, L. Multifunctional envelope-type mesoporous silica nanoparticles for pH-responsive drug delivery and magnetic resonance imaging. *Biomaterials* **2015**, *60*, 111−120.
(37) Webb, B. A.; Chimenti, M.; Jacobson, M. P.; Barber, D. L. Dysregulated pH: a perfect storm for cancer progression. *Nat. Rev. Cancer* **2011**, *11*, 671−677.
(38) Corbet, C.; Feron, O. Tumour acidosis: from the passenger to the driver's seat. *Nat. Rev. Cancer* **2017**, *17*, 577−593.
(39) Yan, J.; Wang, K.; Gui, L.; Liu, X.; Ji, Y.; Lin, J.; Luo, M.; Xu, H.; Lv, J.; Tan, F.; Lin, L.; Yuan, Z. Diagnosing Orthotopic Lung Tumor Using a NTR-Activatable Near-Infrared Fluorescent Probe by Tracheal Inhalation. *Anal. Chem.* **2023**, *95*, 14402−14412.
(40) Chen, X.; Bian, Y.; Li, M.; Zhang, Y.; Gao, X.; Su, D. Activatable Off-on Near-Infrared QCy7-based Fluorogenic Probes for Bioimaging. *Chem.—Asian J.* **2020**, *15*, 3983−3994.
(41) Liu, H. W.; Chen, L.; Xu, C.; Li, Z.; Zhang, H.; Zhang, X. B.; Tan, W. Recent progresses in small-molecule enzymatic fluorescent probes for cancer imaging. *Chem. Soc. Rev.* **2018**, *47*, 7140−7180.
(42) Ouyang, J.; Sun, L.; Zeng, Z.; Zeng, C.; Zeng, F.; Wu, S. Nanoaggregate Probe for Breast Cancer Metastasis through Multispectral Optoacoustic Tomography and Aggregation-Induced NIR-I/II Fluorescence Imaging. *Angew. Chem., Int. Ed. Engl.* **2020**, *59*, 10111−10121.
(43) Huang, G.; Zhao, T.; Wang, C.; Nham, K.; Xiong, Y.; Gao, X.; Wang, Y.; Hao, G.; Ge, W. P.; Sun, X.; Sumer, B. D.; Gao, J. PET imaging of occult tumours by temporal integration of tumour-acidosis signals from pH-sensitive (64)Cu-labelled polymers. *Nat. Biomed. Eng.* **2020**, *4*, 314−324.
(44) Du, H.; Zhao, S.; Wang, Y.; Wang, Z.; Chen, B.; Yan, Y.; Yin, Q.; Liu, D.; Wan, F.; Zhang, Q.; Wang, Y. pH/Cathepsin B Hierarchical-Responsive Nanoconjugates for Enhanced Tumor Penetration and Chemo-Immunotherapy. *Adv. Funct. Mater.* **2020**, *30*, 2003757.

https://doi.org/10.1021/jacsau.4c00356
JACS Au 2024, 4, 2606−2616